PAPER • **OPEN ACCESS**

Highly efficient lateral spin valve device based on graphene/hBN/Fe_3GeTe_2

To cite this article: Jan Bärenfänger *et al* 2025 *2D Mater.* **12** 045008

2D Materials

OPEN ACCESS

RECEIVED
24 April 2025

REVISED
21 July 2025

ACCEPTED FOR PUBLICATION
25 July 2025

PUBLISHED
6 August 2025

PAPER

Highly efficient lateral spin valve device based on graphene/hBN/Fe_3GeTe_2

Jan Bärenfänger[1], Klaus Zollner[2], Lukas Cvitkovich[2], Kenji Watanabe[4], Takashi Taniguchi[5], Stefan Hartl[1], Jaroslav Fabian[2], Jonathan Eroms[1], Dieter Weiss[1] and Mariusz Ciorga[1,3,*]

[1] Institute for Experimental and Applied Physics, University of Regensburg, 93040 Regensburg, Germany
[2] Institute for Theoretical Physics, University of Regensburg, 93040 Regensburg, Germany
[3] Department of Experimental Physics, Faculty of Fundamentals Problems of Technology, Wrocław University of Science and Technology, 50-370 Wrocław, Poland
[4] Research Center for Electronic and Optical Materials, National Institute for Materials Science, 1-1 Namiki, Tsukuba, Ibaraki 305-0044, Japan
[5] Research Center for Materials Nanoarchitectonics, National Institute for Materials Science, 1-1 Namiki, Tsukuba, Ibaraki 305-0044, Japan
[*] Author to whom any correspondence should be addressed.

E-mail: mariusz.ciorga@pwr.edu.pl

Keywords: spin injection, 2D magnets, van der Waals heterostructures

Supplementary material for this article is available online

Abstract

In this work we report efficient out-of-plane spin injection and detection in an all-van der Waals based heterostructure using only exfoliated 2D materials. We demonstrate spin injection by measuring spin-valve and Hanle signals in non-local transport in a stack of Fe_3GeTe_2 (FGT), hexagonal boron nitride (hBN) and graphene layers. FGT flakes form the spin aligning electrodes necessary to inject and detect spins in the graphene channel. The hBN tunnel barrier provides a high-quality interface between the ferromagnetic electrodes and graphene, eliminating the conductivity mismatch problem, thus ensuring efficient spin injection and detection with spin injection efficiencies of up to $P = 40\%$. Our results demonstrate that FGT/hBN/graphene heterostructures form a promising platform for realizing 2D van der Waals spintronic devices.

1. Introduction

Combining two-dimensional (2D) materials into van der Waals (vdW) heterostructures opens up unprecedented possibilities to study novel physical phenomena and to develop new device concepts [1]. Adding magnets to the rich library of vdW materials, comprising metals, insulators, semiconductors, and topological insulators, has invigorated the field of spintronics [2–6]. One of the key issues in spintronics is the efficient generation of spin polarization in non-magnetic materials [7]. Electrical spin injection from ferromagnetic materials has emerged as a highly effective method to achieve this goal. The first reports on electrical spin injection and detection in graphene, by Tombros *et al* in 2007, utilized conventional ferromagnetic Co electrodes with in-plane magnetization and insulating oxide tunnel barriers [8]. This work not only confirmed graphene's potential as an excellent spin transport medium with spin relaxation lengths up to 2 μm, but also revealed the critical role of tunnel barriers in overcoming the conductivity mismatch problem between the highly conductive ferromagnet and graphene. Despite the initial successes, yielding spin injection efficiencies of approximately $P \approx 30\%$ and non-local spin valve signals of up to 130 Ω [9], the fabrication of high-quality, uniform oxide tunnel barriers on graphene proved challenging [8]. The non-uniform growth of these barriers often results in pinholes, effectively short-circuiting the barrier and diminishing spin injection efficiency [8, 10]. Since then, the foundations of spin transport in graphene have been established [11] including also the role of proximity effects [12–16] in order to enhance and manipulate the spin signal [3]. Furthermore, the potential of crystalline hBN as pinhole-free tunnel barriers for spin injection into graphene has been demonstrated [17–24].

The challenges with conventional materials have motivated the exploration of all-vdW heterostructures for graphene spintronics. The unique properties of vdW materials, such as their atomically flat surfaces and perfect crystallinity, as well as their ability to be stacked independently of lattice matching, provide a robust solution to the limitations of conventional material growth techniques, enabling fully crystalline spin transport devices. The discovery of metallic 2D ferromagnets [25] enables the creation of spin injection and detection devices made entirely of vdW materials. Although significant progress has been made in 2D spintronics, existing spin injection and detection platforms often adopt a hybrid approach, combining spin-selective contacts based on 2D ferromagnets with those based on conventional ferromagnets, using an oxide tunnel barrier solely between graphene and the latter [26–28]. To our knowledge, platforms with spin-selective contacts based solely on 2D ferromagnets have not utilized a tunnel barrier so far [29–31]. In both scenarios, the absence of a tunnel barrier between the graphene channel and the 2D ferromagnet leads to low spin injection or detection efficiencies as a result of the conductivity mismatch between both materials. This underscores the necessity of a well-defined tunnel barrier in all-vdW spintronic devices. Furthermore, spin injection and detection have been demonstrated through proximity effects induced by $Cr_2Ge_2Te_6$ on graphene, yielding relatively small non-local signals of up to 0.18 Ω [5].

In this paper, we report on highly efficient spin injection and detection in all-vdW spin transport devices with a hexagonal boron nitride (hBN) tunnel barrier between Fe_3GeTe_2 (FGT) and monolayer graphene. We observe clear spin valve and Hanle signals in non-local transport measurements, from which we determine the spin injection efficiency, spin relaxation times, and spin diffusion constants. To complement our experimental findings, we performed density functional theory (DFT) calculations, providing further insights into the spin transport mechanisms in this promising vdW platform.

2. Experimental details

We observed spin signals in two very similar spin injection devices, sample A and sample B. Here we present the measurement results for sample A, while the measurements for sample B are summarized in the supplementary information (figures S1 and S2). A microscope image of sample A is shown in figure 1(a). The device consists of a monolayer graphene channel with two ferromagnetic contacts on top, composed of an FGT/hBN structure. hBN, FGT and graphene were exfoliated onto p^{++} doped silicon (Si) chips with a 90 nm SiO_2 capping layer [32]. However, the FGT flakes were exfoliated in a glovebox with an O_2 concentration below 0.1 ppm. The widths of the two FGT flakes are 2.6 μm and 1.6 μm for sample A and 2.3 μm and 1.6 μm for sample B. The thicknesses of the injecting and detecting electrodes for sample A are 145 nm and 85 nm, respectively, while for sample B they are 66 nm and 113 nm. The distance between the two FGT flakes, which defines the length of the spin transport channel, is $d = 5$ μm for sample A and 5.6 μm for sample B, measured between the centers of the flakes. The stack was assembled inside the glovebox on a p^{++} doped Si chip with a 285 nm thick layer of dielectric SiO_2 using a standard dry transfer technique employing polycarbonate [33]. The highly doped silicon is used as a global back gate. The graphene was then patterned into a Hall bar using electron beam lithography (EBL) and reactive ion etching . The width of the Hall bar is 3.5 μm. Subsequently, the contacts to the Hall bar and to the ferromagnetic electrodes were prepared using EBL and standard thermal evaporation of Ti(5 nm)/Au(150 nm). A schematic of the completed sample is shown in figure 1(b). The layer sequence of the device thus consists of a mono-layer of graphene on top of the SiO_2 substrate followed by a 0.9 – 1.3 nm thick layer of hBN (measured with atomic force microscopy (AFM)) just below the FGT flakes, which are then covered by another hBN flake as a capping layer. The thin hBN flake acts as a tunnel barrier to ensure good spin injection efficiency [34]. It is worth noting that the samples without a tunnel barrier did not show any spin signal.

All experiments were carried out in a cryostat capable of reaching temperatures as low as 1.5 K, with the sample mounted on a rotating holder that allowed varying the angle between the sample and the applied external magnetic field. Spin injection experiments were performed in a standard non-local configuration (see figure 1(c)), with the charge current flowing between one of the FM contacts and a reference non-magnetic contact at the end of the mesa [35]. The charge current flowing through the FGT/hBN/graphene structure generates a spin accumulation in graphene, which diffuses away from the junction in all directions (red shaded region in figure 1(c)). The spin accumulation can then be detected by the second FGT/hBN contact, placed at a distance d from the injecting contact, outside the charge current path. The non-local voltage measured between the detector and the reference contact serves as a measure of the spin accumulation beneath the detector. The electronic measurements were carried out using a Yokogawa 7651 as the DC current source and a Keithley 2400 as a back gate voltage source. The measured non-local voltage was amplified by a FEMTO DLPVA-101 voltage amplifier that was connected to a SynkTek MCL1-540

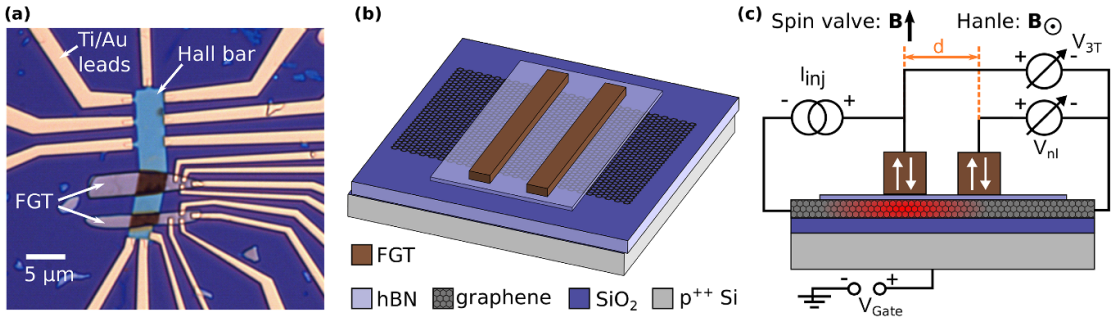

Figure 1. (a) Optical micrograph of sample A. (b) Schematic of the samples. The encapsulating hBN is omitted for clarity. (c) Schematic of the non-local measurement setup. For the spin valve (Hanle) measurements the external magnetic field was swept out-of-plane (in-plane) along (perpendicular to) the easy-axis of the FGT electrodes.

multi-channel data acquisition system. Voltages at other voltage probes, for example the three-terminal voltage V_{3T}, were measured with the SynkTek data acquisition system alone, without an amplifier. Since FGT has its magnetic easy-axis out-of-plane, the non-local spin valve experiments were all performed by sweeping the external magnetic field in this direction. For the Hanle measurements, the external magnetic field was swept in-plane, along the long axis of the spin contacts, perpendicular to the transport channel.

3. Results and discussion

3.1. Electrical characterization

Before describing the results of the spin measurements, we first discuss the electrical characterization of the device components. We characterized the graphene channel by measuring its sheet resistance R_S as a function of the back gate voltage, determining the charge neutrality point at $V_g = -4$ V, in the Hall bar section of the device (see figure 2(a)). From this measurement, mobilities of up to 11 000 $\mathrm{cm^2\,Vs^{-1}}$ were extracted, consistent with the results of the Hall measurements (see figure S3 in the supplementary information). In figure 2(b) we show the I–V-curve of the injection electrode, as a function of the three-terminal voltage. The zero-bias resistance-area product $R_{3T,\,0V}A$ characterizes the tunnel barrier, according to Britnell *et al* [36]. The measured $R_{3T,0V}A \sim 95\,\mathrm{k\Omega}\cdot\mu\mathrm{m}^2$ corresponds to the hBN flake being two layers thick, which is consistent with the AFM measurements within the measurement accuracy. Furthermore, the switching behavior of the injecting FGT electrode was monitored by measuring the transverse voltage across the FGT flake, while a constant current was sent from the injecting FGT electrode into the graphene (see figure 2(c)). In a ferromagnet, the transverse voltage is composed of the regular and the anomalous Hall voltage, with the latter being proportional to the magnetization of the ferromagnetic ($R_{xy} = R_{RH} + R_{AH} = R_0\mu_0\cdot H + R_S\cdot M$, [37]). Therefore, we can attribute a sharp step in the transverse anomalous Hall voltage to the abrupt switching of the magnetization in our injecting FGT electrode. This switching is consistent with the switching of the non-local voltage in spin-valve measurements, as described later.

3.2. Non-local spin valve

Non-local spin-valve measurements are a standard way of detecting spin accumulation in lateral spin injection devices [8, 35, 38, 39]. Here, a magnetic field is swept along the easy-axis of the spin electrodes, which in our case is oriented out-of-plane, and the non-local voltage V_{nl} is measured at the detector, with a current flowing in the injector circuit. Changes in V_{nl} are observed whenever the magnetization of one of the contacts switches, leading to a transition between parallel and anti-parallel magnetization configurations in the two spin aligning electrodes. In figure 3(a) we show a typical spin valve trace, where we plot V_{nl} normalized by the injection current I as a non-local resistance $R_{nl} = V_{nl}/I$. The amplitude of the switching ΔR_{nl} serves as a measure of the generated spin accumulation and is given by [7, 40]

$$\Delta R_{nl} = \frac{P_{inj}P_{det}R_S\lambda_s}{w}\exp\left(-\frac{d}{\lambda_s}\right). \qquad (1)$$

In the above equation, λ_s is the spin diffusion length, w is the width of the channel, and P_{inj} and P_{det} are the spin injection and detection efficiency, respectively. These efficiencies are defined as the spin polarization of the injected current directly underneath the given contact when the contact is used as an injector. Assuming the same interfaces at the injector and detector contacts and for low injection currents, one can take $P_{inj} \approx P_{det} = P$. In general, however, P_{inj} can depend on the injection current, leading to a current dependence of the measured signal, as shown in figure 3(b). We plot here ΔR_{nl} measured at $T = 1.5$ K for gate voltages $V_g = 45$ V and $V_g = -45$ V, corresponding to electron and hole transport in graphene,

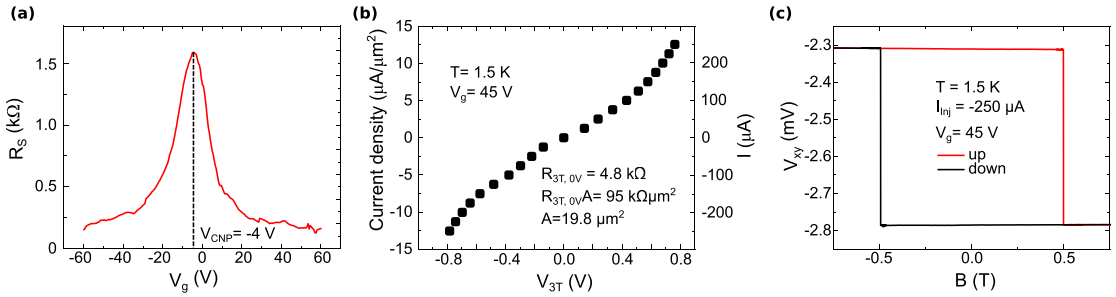

Figure 2. Electronic characterization of the device. (a) Sheet resistance R_S of the graphene channel in the reference area as a function of the back gate voltage. The measurements have been carried out at $T = 1.5$ K and with $I = 50$ μA. (b) Characterization of the hBN tunnel barrier. The current density is plotted against the measured three-terminal voltage at the injecting electrode, which constitutes a voltage dropped across the tunnel barrier contact. The current density, shown on the left side, presents the current normalized by the area of the FGT/hBN contact. (c) Transversal voltage measured across the FGT flake, while sweeping the external magnetic field out-of-plane during the spin valve measurements shown in figure 3(a). Red (black) line corresponds to the up (down) sweep. The observed switching corresponds to the switching of magnetization in the FGT flake.

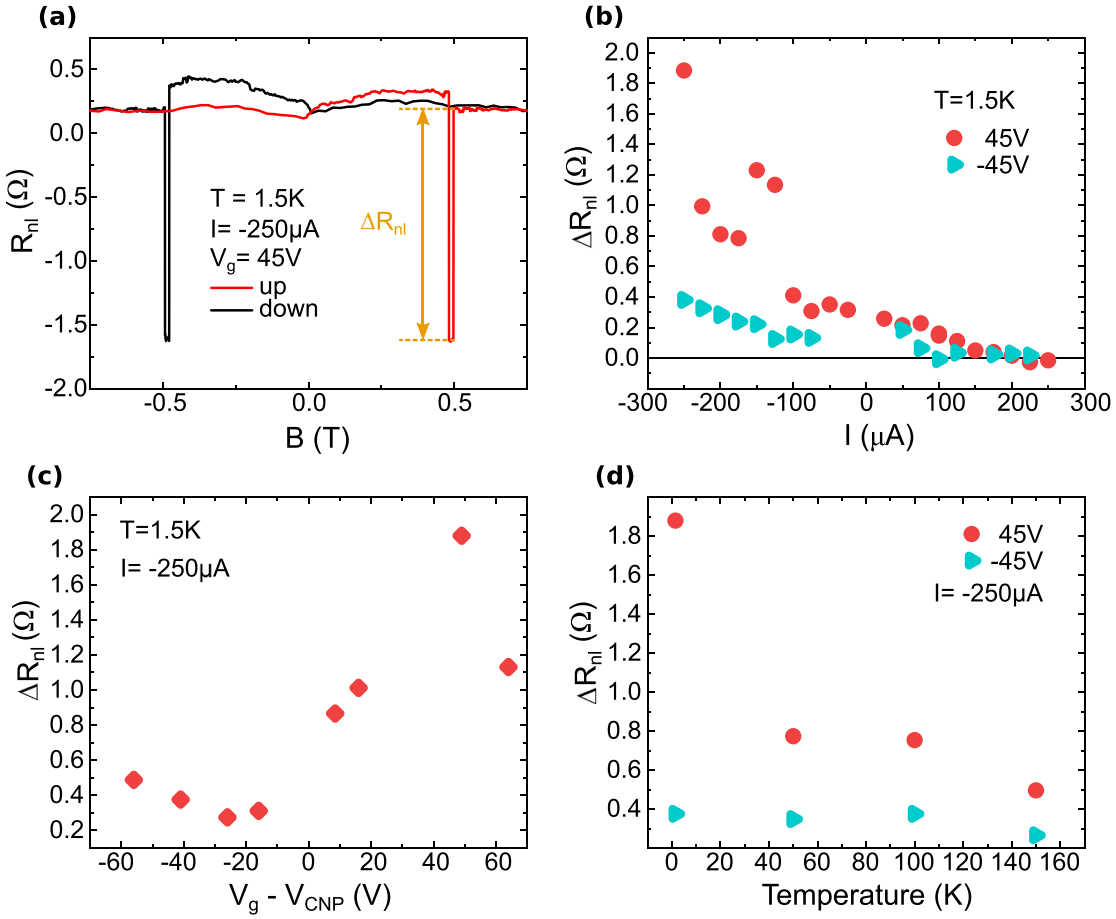

Figure 3. (a) Non-local spin valve measurement at $T = 1.5$ K, $V_g = 45$ V and a current of $I = -250$ μA. The dip of the non-local signal at low magnetic fields is clearly discernible. In yellow, the height of the non-local signal ΔR_{nl} is shown. (b) Current, (c) back gate voltage and (d) temperature dependence of the non-local signal height in the electron ($V_g = 45$ V) and hole ($V_g = -45$ V) regime.

respectively. For both carrier polarities, ΔR_{nl} is higher for a negative bias, corresponding to injection of spin-polarized electrons from FGT into graphene or extraction of spin-polarized holes, respectively, and decreases almost monotonically, as the injection current is changed towards positive values. For very high positive currents at $T = 1.5$ K we even observe an inversion of the spin signal in the electron regime. Such behavior is typically driven by a change in the sign of P_{inj} with bias, indicating an inversion of spin polarization around the Fermi level of the ferromagnetic material. This phenomenon has been observed previously in both conventional graphene spin valve devices [41, 42] and in III–V materials [38].

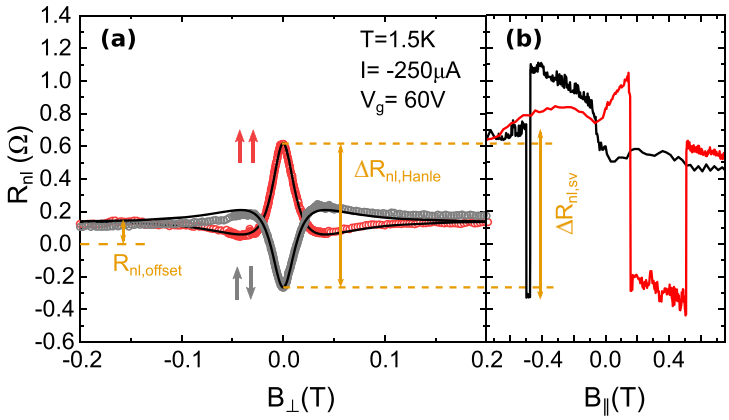

Figure 4. (a) Hanle signal for parallel (red) and anti-parallel (gray) magnetization alignment of the FGT electrodes. Fits to the measurements are shown as black curves. The non-local Hanle signal height at $B = 0$ T is $\Delta R_{\text{nl, Hanle}} = 0.88\,\Omega$. (b) Non-local spin valve measurement for the same measurement parameters. The spin valve height is $\Delta R_{\text{nl, spin valve}} = 1.13\,\Omega$. The magnetic field is swept perpendicular and parallel to the magnetization direction of FGT in (a) and (b), respectively.

In recent experiments with Fe_5GeTe_2, it was shown that Fe_5GeTe_2 had an opposite spin polarization compared to that observed in Co electrodes for the entire range of bias currents used [26]. In our experiments, the sign reversal of the spin valve signal is a result of the sign change in the tunneling density of states (TDOS) in our structure, as will be discussed later in more detail.

In the entire range of bias currents, the signal is much stronger for electrons than for holes, which is confirmed by plotting ΔR_{nl} as a function of gate voltage, see figure 3(c). Additionally, it can be observed that ΔR_{nl} increases with the absolute value of V_{g}. Similar behavior was also observed at higher temperatures, as can be seen in the supplementary figure S4. In figure 3(d) we plot ΔR_{nl} as a function of T for $I = -250\,\mu$A, showing a general trend of decreasing spin signal with increasing T. Whereas the current dependence of ΔR_{nl} can be linked to the bias dependence of P_{inj}, explaining its gate and temperature dependence requires information about gate and T-dependence of P_{inj}, λ_{s}, and R_{s}. To experimentally determine λ_{s} and P_{inj}, we performed Hanle measurements, investigating spin precession in an external transversal magnetic field, which we will discuss in the next section.

Apart from a clear spin-valve pattern, we also observed another feature in the spin-valve measurements, namely a dip in the non-local signal at low magnetic fields, see figure 3(a) and figure S5 in the supplementary information. Such a dip is typically associated with the presence of magnetic moments in a graphene channel, which introduce relaxation of spin currents through exchange coupling [43–45]. Given that our samples were fabricated in an inert atmosphere and capped with hBN, and were not subjected to any hydrogenation [43, 44] or annealing [45] processes, which are reported to induce magnetic moments, we cannot provide an explanation for the origin of these magnetic moments. However, the results of the Hanle measurements, discussed below, are also consistent with the presence of magnetic moments in the channel.

3.3. Hanle signal

In Hanle measurements, the external magnetic field is applied transversely to the orientation of the injected spins, inducing their precession as they travel from the injector to the detector [8]. As a result of diffusive motion and spin relaxation, the spins dephase and depolarize, which is reflected in the measured V_{nl} [7]. In figure 4(a) we plot a Hanle signal for the injection current $I = -250\,\mu$A, at a temperature $T = 1.5$ K and a back-gate voltage of $V_{\text{g}} = 60$ V for the anti-parallel (gray) and parallel (red) magnetization configuration of the two ferromagnetic electrodes of sample A. The similar plot for sample B can be seen in figure S1(d). Since the spins injected from FGT are polarized out of plane, we applied an external in-plane magnetic field, parallel to the long axis of FGT flakes. The difference of the signal measured for parallel and anti-parallel sweeps at $B = 0$ T gives $\Delta R_{\text{nl,Hanle}} = 0.88\,\Omega$, which is slightly lower than the corresponding spin valve signal $\Delta R_{\text{nl, sv}} = 1.13\,\Omega$ (see figure 4(b)). This small discrepancy between the Hanle and spin valve signals may be attributed to the presence of magnetic moments, which reduce the spin signal at low magnetic fields, thereby reducing the height of the Hanle curve. This observation is consistent with the findings of the non-local spin valve measurements, which also indicated the presence of magnetic moments. It is noteworthy that these magnetic moments are believed to be extrinsic and not associated with the

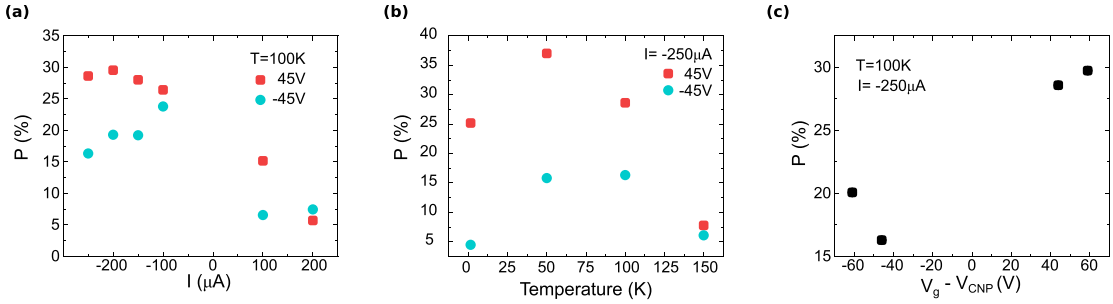

Figure 5. (a) Current, (b) temperature and (c) gate voltage dependence of the spin injection efficiency P obtained from fits to the Hanle curves. Error bars, determined as the fitting errors, are in most cases smaller than the size of the symbols.

FGT electrodes. However, we cannot rule out a hysteresis of the signal due to the measurement procedure, as we first recorded the spin valves for all currents and back gate voltages and afterwards performed the Hanle sweeps. The small hysteresis with respect to the current or gate voltage cannot be excluded and could potentially lead to a smaller signal in the Hanle curves. There is also a small asymmetry between the signal in parallel and anti-parallel configuration, which we cannot account for at the moment.

At finite transverse fields, we clearly observe oscillations of the signal as a result of spin precession and simultaneous decay of the signal as a result of spin dephasing. At a sufficiently large magnetic field $B \gtrsim 0.2$ T, spins depolarize through dephasing, the spin signal approaches zero, and the measured non-local resistance $R_{\mathrm{nl,\,offset}}$ constitutes the non-local baseline resistance [46, 47]. The solid lines in figure 4(a) are fitting curves based on the steady-state solution of the spin drift-diffusion equation [7] $\frac{\partial \boldsymbol{\mu}_\mathrm{s}}{\partial t} = \boldsymbol{\mu}_\mathrm{s} \times \boldsymbol{\omega_L} + D_\mathrm{s}\nabla^2\boldsymbol{\mu}_\mathrm{s} - \frac{\boldsymbol{\mu}_\mathrm{s}}{\tau_\mathrm{s}}$, with the boundary condition at the injector $e^2 D_\mathrm{s}\nu(E_\mathrm{F})\nabla\boldsymbol{\mu}_\mathrm{s} = P_\mathrm{inj}\boldsymbol{j}$. In the above equations, μ_s indicates spin accumulation generated by the injection current density $\boldsymbol{j}$, which at the detector is measured as a non-local voltage $V_\mathrm{nl} = -P_\mathrm{det}\mu_\mathrm{s}(d)$, D_s is the spin diffusion constant, τ_s spin relaxation time, $\boldsymbol{\omega_L} = \frac{g^*\mu_\mathrm{B}\boldsymbol{B}}{\hbar}$ is the Larmor frequency at the external magnetic field $\boldsymbol{B}$, with $g^* = 2$ being the Landé factor, $\nu(E_\mathrm{F})$ is the DOS at the Fermi level, μ_B is the Bohr's magneton and $\hbar$ the reduced Planck's constant. From the fitting curves, we obtain the values of P, D_s and τ_s, with the latter two giving the spin diffusion length $\lambda_\mathrm{s} = \sqrt{D_\mathrm{s}\tau_\mathrm{s}}$. The extracted value of P is $P = \sqrt{P_\mathrm{inj}P_\mathrm{det}}$. To minimize errors in fitting these three variables, we first fitted the normalized Hanle data $(R_{\mathrm{nl,\,B}} - R_{\mathrm{nl,\,offset}})/(R_{\mathrm{nl,\,0T}} - R_{\mathrm{nl,\,offset}})$ to extract τ_s and D_s from the shape of the curves and then we fitted the raw data with the extracted values from the normalized fits. Therefore, P was the only variable in the second fit. As can be seen in figure 4(a) the fits (shown as a black line) match the experimental data quite well. Fitting the parallel Hanle curve gives $\tau_\mathrm{s} = 0.447$ ns, $D_\mathrm{s} = 0.0210\ \frac{\mathrm{m}^2}{\mathrm{s}}$, and $P = 18.4\%$, whereas we obtain $\tau_\mathrm{s} = 0.415$ ns, $D_\mathrm{s} = 0.0199\ \frac{\mathrm{m}^2}{\mathrm{s}}$, and $P = 18.3\%$ in the anti-parallel configuration.

We performed Hanle measurements in the parallel configuration for different injection currents, back gate voltages and at different temperatures. The full set of results for sample A and B can be found in the supplementary figures S6 and S2, respectively. The fitting results for P of sample A are summarized in figure 5. In the following section, we discuss in more detail the obtained results.

3.4. Discussion

As can be seen in figure 5, we have obtained a fairly high injection efficiency, reaching up to 40%, which is significantly higher than that reported for structures without tunnel barriers [29]. However, this is a low estimate of P_inj. When linearly extrapolating $P_\mathrm{det}(1.5\,\mathrm{K}) = P(I = 0, \mathrm{T} = 1.5\mathrm{K})$ to be $\approx 17\%$, the spin injection efficiency is estimated to be $P_\mathrm{inj}(-200\,\mu\mathrm{A}, 45\,\mathrm{V}, 1.5\,\mathrm{K}) = 93\%$. Consistent with the spin valve signal ΔR_nl, P is larger for the negative back gate voltages, i.e. in the electron regime, as shown in figure 5(c), and for negative injection currents, i.e. for the case of electron injection. P decreases, while sweeping the injection current from negative to positive values as illustrated in figure 5(a). As bias affects only the injector, the decrease in P with current is attributed to a decrease of P_inj. P also decreases with increasing temperature for $T \geqslant 50$ K, although at $T = 1.5$ K, P is lower than at $T = 50$ K, both in the electron and hole regime, as shown in figure 5(b).

In order to properly interpret the current dependence of the spin injection efficiency (as shown in figure 5(a)), it is helpful to have some knowledge about the spin polarization of Fe_3GeTe_2. To this end, we performed DFT calculations of the electronic band structure of the bulk FGT (see the supplementary information IV for details), including the spin-resolved DOS. A measure for the degree of spin polarization of the injected current is the

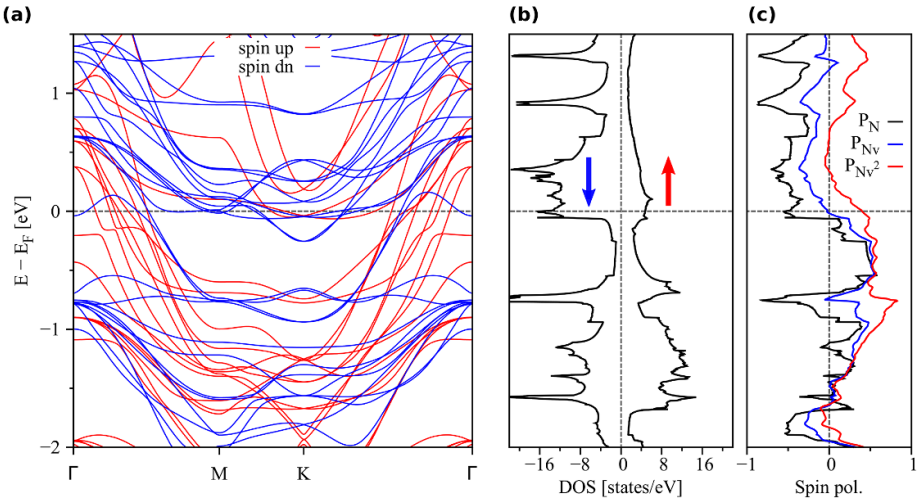

Figure 6. (a) DFT-calculated band structure of bulk Fe_3GeTe_2. Red (blue) lines correspond to spin up (down). (b) The corresponding spin-resolved density of states. Negative (positive) values for the DOS reflect a spin down (up) polarization, as indicated by the blue (red) arrow. (c) Calculated results for the spin polarization P_N, P_{Nv} and P_{Nv^2}.

tunneling density of states (TDOS), which is defined via the product of DOS and the velocity of the Bloch bands [48]. It should be noted that this calculation does not take into account any properties of the interface, the barrier or the second contact. Based on spin-resolved DOS, $N_{\uparrow/\downarrow}$, and Bloch band velocities in the z-direction (perpendicular to the Fe_3GeTe_2 layers), v_z, we calculate the DOS spin polarization P_N of the bulk FGT and the TDOS spin polarization P_{Nv} and P_{Nv^2} as follows [48]:

$$P_N = \frac{N_\uparrow - N_\downarrow}{N_\uparrow + N_\downarrow}, \tag{2}$$

$$P_{Nv} = \frac{\langle Nv_z\rangle_\uparrow - \langle Nv_z\rangle_\downarrow}{\langle Nv_z\rangle_\uparrow + \langle Nv_z\rangle_\downarrow} \tag{3}$$

$$P_{Nv^2} = \frac{\langle Nv_z^2\rangle_\uparrow - \langle Nv_z^2\rangle_\downarrow}{\langle Nv_z^2\rangle_\uparrow + \langle Nv_z^2\rangle_\downarrow}. \tag{4}$$

In figures 6(a) and (b) we show the calculated FGT band structure and its spin-resolved DOS, respectively. Additionally, the spin polarization P_N, together with the TDOS P_{Nv} and P_{Nv^2} are shown in figure 6(c). We note that at the Fermi level E_F and at higher energies, the DOS is highly spin-polarized with the majority of spin-down states. However, slightly below E_F, the DOS decreases, particularly for spin-down states. Both P_N and P_{Nv} change sign below E_F. In contrast to this, P_{Nv^2} tends to stay positive in the close vicinity of E_F, indicating that the current is dominated by the spin-up charge carriers. However, the degree of spin polarization of P_{Nv^2} decreases towards larger energies. In the experiment, we tune the alignment of the Fermi-level of graphene and FGT by changing the bias across the junction and we note that the calculated decrease of P_{Nv^2} towards larger energies is very consistent with the measured decrease of spin injection efficiency towards larger positive currents, shown in figure 5(a).

In order to obtain a comprehensive understanding of the tunneling, it is necessary to calculate the coherent tunneling for the entire FGT/hBN/hBN/graphene structure. This calculation requires precise knowledge of the band structure and the exact twist angles of each layer. However, as we lack access to this structural information, and given the focus of this paper on the experimental realization of efficient spin injection and detection in all vdW heterostructures, these calculations cannot be performed and are beyond the scope of the presented work. Nevertheless, a change of sign at or near the E_F is evident for all calculated spin polarizations P_N, and P_{Nv}, and P_{Nv^2} of FGT, which might provide an explanation for the current dependence of the non-local signal height (see figure 3(b)) and the spin injection efficiency (see figure 5(a)).

Let us now discuss the obtained spin transport parameters. The extracted values for τ_s are in the range from ∼300 to ∼600 ps and D_s spans from ∼0.004 to ∼0.04 $m^2 s^{-1}$. There is no clear dependence of both variables on current and on gate voltage. However, fit results of τ_s and D_s both suggest larger values for negative than for positive back gate voltages, i.e. in the hole conduction regime (see figure S6). Furthermore, a small dependence of τ_s and D_s on temperature is observed. Whereas the values extracted for $T = 1.5$ K are larger than at $T = 50$ K, for $T \geqslant 50$ K the spin relaxation time increases from $\tau_s = 0.3$ ns at $T = 50$ K to 0.5 ns at $T = 150$ K in the electron regime and a similar effect can also be seen in the hole regime (see figure S6). Also D_s increases with temperature in a similar way as τ_s, so the calculated spin diffusion length $\lambda_s = \sqrt{D_s \tau_s}$ doubles from

1.5 μm to 3.1 μm in the electron regime and increases from 2.24 μm to 2.78 μm in the hole regime.

Surprisingly, the extracted values of D_s are significantly lower than the values of the charge diffusion constant D_c at the same temperatures and gate voltages, as obtained from transport measurements, which are in the range $0.08 - 0.12\,m^2\,s^{-1}$ (see supplementary figure S8). This discrepancy between the charge and spin diffusion constants and the temperature dependence of τ_s could be explained by the presence of magnetic moments, which would be consistent with the spin valve measurements. Resonant scattering at magnetic impurities introduces a temperature-dependent scattering rate [49] and results in narrower Hanle curves due to the additional exchange field [43]. This exchange field can be taken into account in the Hanle curve fitting, taking a larger effective g-factor $g^* > 2$. During the above-described fitting of the Hanle curves, a constant g-factor of $g^* = 2$ was assumed, which in the presence of magnetic moments results in incorrect values of D_s. To correct for this, we performed an alternative fitting, where we fixed $D_s = D_c$ and extracted from the fitting the effective g-factor. However, this resulted in very large values of the effective g-factor, reaching as high as $g^*_{eff} = 23$. This would indicate the presence of a substantial exchange field or a significant amount of magnetic moments in the graphene channel, whose origin is unknown to us.

Another explanation for the peculiar temperature dependence of τ_s and D_s, and the low values of D_s, could be provided by the assumption, that under contacts both τ_s and D_s are strongly suppressed because of the influence of the ferromagnetic FGT. As the fitting was performed assuming uniform τ_s and D_s throughout the channel, the extracted values of both parameters could be underestimated. As with increasing temperature the magnetization of FGT decreases (see figure S9), so does its possible detrimental effect on the spin dynamics in graphene. As a result, the extracted τ_s and D_s would increase. In order to investigate a potential magnetic proximity effect [13, 15] at the FGT/hBN/graphene interface, we performed DFT calculations with a two-layer hBN tunnel barrier (see supplementary information IV for details). In the calculated band structure of the heterostructure, the Dirac states of graphene remain spin-degenerate, and no magnetic moments are induced. Consequently, a proximity effect in graphene due to the FGT can be ruled out and cannot explain the discrepancy of D_c and D_s.

4. Conclusion

In conclusion, we report on efficient electrical spin transport and spin precession in an all-vdW 2D device. Non-local signals are as large as $\Delta R_{nl} \approx 1.9\,\Omega$, showing a strong current dependence, and even leading to the inversion of the signal. The clear Hanle signal allowed for a full gate-, temperature-, and current-dependent characterization of the spin transport properties. A low estimate of the spin injection efficiencies results in $P(-200\,\mu A, 45\,V, 1.5\,K) = 40\,\%$. The observed bias dependence of the spin injection efficiency, and the inversion of the spin valve signal are consistent with the calculated TDOS. The presence of a small dip in the non-local spin valve measurements as well as the discrepancy between D_s and D_c suggest the presence of magnetic moments, whose origin, however, remains unknown.

Overall, this work demonstrates the potential of all-vdW heterostructures for realizing high-performance spintronic devices. Future advancements in this field could exploit the precise angular alignment of the constituent vdW materials. This concept, often termed as *twistronics* [50, 51], is a powerful tool to tune the interface properties of a given heterostructure. The twist angle between stacked layers can be a decisive parameter that influences proximity effects and the resulting band structure of the heterostructure [52–55]. Consequently, angle-dependent studies on similar all-vdW spin transport devices would be highly valuable to unravel and control the spin injection and detection mechanisms. Ultimately, utilizing the twist-angle between vdW materials could pave the way for realizing fully coherent tunneling spintronic devices with unprecedented spin injection efficiencies.

Data availability statement

The data that support the findings of this study are openly available at the following URL/DOI: https://doi.org/10.5283/epub.76433.

Acknowledgments

J B, J E, K Z, L C and J F gratefully acknowledge support from the Deutsche Forschungsgemeinschaft (DFG, German Research Foundation) SFB 1277 (Project No. 314695032, sub-Project B07, A09), SPP 2244 (Project No. 443416183), the EU Graphene Flagship project 2DSPIN-TECH (Project No. 101135853), and FLAGERA project 2DSOTECH. K.W. and T.T. acknowledge support from the JSPS KAKENHI (Grant Numbers 21H05233 and 23H02052) , the CREST (JPMJCR24A5), JST and World Premier International Research Center Initiative (WPI), MEXT, Japan. M. C. acknowledges support by the National Science Centre, Poland, Project No. 2022/45/B/ST5/04292 of OPUS-23 call. We would also like to thank C Strunk for facilitating access to the reactive ion etching system.

ORCID iDs

Jan Bärenfänger 0009-0006-1900-8047
Klaus Zollner 0000-0002-6239-3271
Lukas Cvitkovich 0000-0003-2453-507X
Kenji Watanabe 0000-0003-3701-8119
Takashi Taniguchi 0000-0002-1467-3105
Jaroslav Fabian 0000-0002-3009-4525
Jonathan Eroms 0000-0003-2212-9537
Dieter Weiss 0000-0002-9630-9787
Mariusz Ciorga 0000-0003-2441-7874

References

[1] Novoselov K S, Mishchenko A, Carvalho A and Castro Neto A H 2016 2D materials and van der Waals heterostructures *Science* **353** aac9439
[2] Deiseroth H-J, Aleksandrov K, Reiner C, Kienle L and Kremer R K 2006 Fe_3GeTe_2 and Ni_3GeTe_2– two new layered transition–Metal compounds: crystal structures, HRTEM investigations and magnetic and electrical properties *Eur. J. Inorg. Chem.* **2006** 1561
[3] Sierra J F, Fabian J, Kawakami R K, Roche S and Valenzuela S O 2021 van der Waals heterostructures for spintronics and opto-spintronics *Nat. Nanotechnol.* **16** 856
[4] Li Y, Yang B, Xu S, Huang B and Duan W 2022 Emergent phenomena in magnetic two-dimensional materials and van der Waals heterostructures *ACS Appl. Electron. Mater.* **4** 3278
[5] Yang H, Gobbi M, Herling F, Pham V T, Calavalle F, Martin-Garcia B, Fert A, Hueso L E and Casanova F 2025 A seamless graphene spin valve based on proximity to van der Waals magnet $Cr_2Ge_2Te_6$ *Nat. Electron.* **8** 15
[6] Huang S *et al* 2025 Giant magnetoresistance induced by spin-dependent orbital coupling in Fe_3GeTe_2/graphene heterostructures *Nat. Commun.* **16** 2866
[7] Fabian J, Matos-Abiague A, Ertler C, Stano P and Žutic I 2007 Semiconductor spintronics *Acta Phys. Slovaca* **57** 565
[8] Tombros N, Jozsa C, Popinciuc M, Jonkman H T and van Wees B J 2007 Electronic spin transport and spin precession in single graphene layers at room temperature *Nature* **448** 571
[9] Han W, Pi K, McCreary K M, Li Y, Wong J J I, Swartz A G and Kawakami R K 2010 Tunneling spin injection into single layer graphene *Phys. Rev. Lett.* **105** 167202
[10] Wang W H, Han W, Pi K, McCreary K M, Miao F, Bao W, Lau C N and Kawakami R K 2008 Growth of atomically smooth MgO films on graphene by molecular beam epitaxy *Appl. Phys. Lett.* **93** 183107
[11] Avsar A, Ochoa H, Guinea F, Özyilmaz B, van Wees B J and Vera-Marun I J 2020 Colloquium: spintronics in graphene and other two-dimensional materials *Rev. Mod. Phys.* **92** 021003
[12] Hallal A, Ibrahim F, Yang H, Roche S and Chshiev M 2017 Tailoring magnetic insulator proximity effects in graphene: first-principles calculations *2D Mater.* **4** 025074
[13] Zollner K, Gmitra M, Frank T and Fabian J 2016 Theory of proximity-induced exchange coupling in graphene on hBN/(Co, Ni) *Phys. Rev. B* **94** 155441
[14] Yang H X, Hallal A, Terrade D, Waintal X, Roche S and Chshiev M 2013 Proximity effects induced in graphene by magnetic insulators: first-principles calculations on spin filtering and exchange-splitting gaps *Phys. Rev. Lett.* **110** 046603
[15] Zollner K and Fabian J 2022 Engineering proximity exchange by twisting: reversal of ferromagnetic and emergence of antiferromagnetic dirac bands in Graphene/$Cr_2Ge_2Te_6$ *Phys. Rev. Lett.* **128** 106401
[16] Yang H, Martín-García B, Kimák J, Schmoranzerová E, Dolan E, Chi Z, Gobbi M, Němec P, Hueso L E and Casanova F 2024 Twist-angle-tunable spin texture in WSe_2/graphene van der Waals heterostructures *Nat. Mater.* **23** 1502
[17] Gurram M, Omar S and van Wees B J 2017 Bias induced up to 100% spin-injection and detection polarizations in ferromagnet/bilayer-hBN/graphene/hBN heterostructures *Nat. Commun.* **8** 248
[18] Gurram M, Omar S, Zihlmann S, Makk P, Schönenberger C and van Wees B J 2016 Spin transport in fully hexagonal boron nitride encapsulated graphene *Phys. Rev. B* **93** 115441
[19] Yamaguchi T, Inoue Y, Masubuchi S, Morikawa S, Onuki M, Watanabe K, Taniguchi T, Moriya R and Machida T 2013 Electrical spin injection into graphene through monolayer hexagonal boron nitride *Appl. Phys. Express* **6** 073001
[20] Singh S, Katoch J, Xu J, Tan C, Zhu T, Amamou W, Hone J and Kawakami R 2016 Nanosecond spin relaxation times in single layer graphene spin valves with hexagonal boron nitride tunnel barriers *Appl. Phys. Lett.* **109** 122411
[21] Kamalakar M V, Dankert A, Bergsten J, Ive T and Dash S P 2014 Enhanced tunnel spin injection into graphene using chemical vapor deposited hexagonal boron nitride *Sci. Rep.* **4** 6146
[22] Fu W, Makk P, Maurand R, Bräuninger M and Schönenberger C 2014 Large-scale fabrication of BN tunnel barriers for graphene spintronics *J. Appl. Phys.* **116** 074306
[23] Kamalakar M V, Dankert A, Kelly P J and Dash S P 2016 Inversion of spin signal and spin filtering in ferromagnet|hexagonal boron nitride-graphene van der Waals heterostructures *Sci. Rep.* **6** 21168
[24] Gurram M, Omar S, Zihlmann S, Makk P, Li Q C, Zhang Y F, Schönenberger C and Van Wees B J 2018 Spin transport in two-layer-CVD-hBN/graphene/hBN heterostructures *Phys. Rev. B* **97** 045411
[25] Deng Y *et al* 2018 Gate-tunable room-temperature ferromagnetism in two-dimensional Fe_3GeTe_2 *Nature* **563** 94
[26] Zhao B *et al* 2023 A room-temperature spin-valve with van der Waals ferromagnet Fe_5GeTe_2/Graphene heterostructure *Adv. Mater.* **35** e2209113
[27] Zhao B, Karpiak B, Hoque A M, Dhagat P and Dash S P 2023 Strong perpendicular anisotropic ferromagnet Fe_3GeTe_2/graphene van der Waals heterostructure *J. Phys. D: Appl. Phys.* **56** 094001
[28] Ngaloy R *et al* 2024 Strong in-plane magnetization and spin polarization in $(Co_{0.15}Fe_{0.85})_5GeTe_2$/graphene van der Waals heterostructure spin-valve at room temperature *ACS Nano* **18** 5240
[29] He X, Zhang C, Zheng D, Li P, Xiao J Q and Zhang X 2023 Nonlocal spin valves based on Graphene/Fe_3GeTe_2 van der Waals heterostructures *ACS Appl. Mater. Interfaces* **15** 9649
[30] Pan H, Zhang C, Shi J, Hu X, Wang N, An L, Duan R, Deb P, Liu Z and Gao W 2023 Room-temperature lateral spin valve in Graphene/Fe_3GaTe_2 van der Waals heterostructures *ACS Mater. Lett.* **5** 2226
[31] Liao X, Liu X-Y, Wang A-Q, Yin Q, Zhao T-Y and Liao Z-M 2024 Nonlinear valley and spin valves in bilayer graphene *Phys. Rev. Appl.* **22** 054078
[32] HBN was grown by a high pressure technique. FGT was bought from HQ graphene and graphene was exfoliated from Flaggy Flakes natural graphite bought from NGS Naturgraphit GmbH
[33] Pizzocchero F, Gammelgaard L, Jessen B S, Caridad J M, Wang L, Hone J, Bøggild P and Booth T J 2016 The hot pick-up technique for batch assembly of van der Waals heterostructures *Nat. Commun.* **7** 11894
[34] Schmidt G, Ferrand D, Molenkamp L W, Filip A T and van Wees B J 2000 Fundamental obstacle for electrical spin injection from a ferromagnetic metal into a diffusive semiconductor *Phys. Rev. B* **62** R4790
[35] Johnson M and Silsbee R H 1985 Interfacial charge-spin coupling: injection and detection of spin magnetization in metals *Phys. Rev. Lett.* **55** 1790
[36] Britnell L *et al* 2012 Electron tunneling through ultrathin boron nitride crystalline barriers *Nano Lett.* **12** 1707

[37] Nagaosa N, Sinova J, Onoda S, MacDonald A H and Ong N P 2010 Anomalous hall effect *Rev. Mod. Phys.* **82** 1539
[38] Lou X, Adelmann C, Crooker S A, Garlid E S, Zhang J, Reddy K S M, Flexner S D, Palmström C J and Crowell P A 2007 Electrical detection of spin transport in lateral ferromagnet-semiconductor devices *Nat. Phys.* **3** 197
[39] Ciorga M, Einwanger A, Wurstbauer U, Schuh D, Wegscheider W and Weiss D 2009 Electrical spin injection and detection in lateral all-semiconductor devices *Phys. Rev. B* **79** 165321
[40] Oltscher M, Ciorga M, Utz M, Schuh D, Bougeard D and Weiss D 2014 Electrical spin injection into high mobility 2D systems *Phys. Rev. Lett.* **113** 236602
[41] Ringer S, Rosenauer M, Völkl T, Kadur M, Hopperdietzel F, Weiss D and Eroms J 2018 Spin field-effect transistor action via tunable polarization of the spin injection in a Co/MgO/graphene contact *Appl. Phys. Lett.* **113** 132403
[42] Zhu T, Singh S, Katoch J, Wen H, Belashchenko K, Žutić I and Kawakami R K 2018 Probing tunneling spin injection into graphene via bias dependence *Phys. Rev. B* **98** 054412
[43] McCreary K M, Swartz A G, Han W, Fabian J and Kawakami R K 2012 Magnetic moment formation in graphene detected by scattering of pure spin currents *Phys. Rev. Lett.* **109** 186604
[44] Wojtaszek M, Vera-Marun I J, Maassen T and van Wees B J 2013 Enhancement of spin relaxation time in hydrogenated graphene spin-valve devices *Phys. Rev. B* **87** 081402
[45] Birkner B, Pachniowski D, Sandner A, Ostler M, Seyller T, Fabian J, Ciorga M, Weiss D and Eroms J 2013 Annealing-induced magnetic moments detected by spin precession measurements in epitaxial graphene on SiC *Phys. Rev. B* **87** 081405
[46] Bakker F L, Slachter A, Adam J P and Van Wees B J 2010 Interplay of peltier and seebeck effects in nanoscale nonlocal spin valves *Phys. Rev. Lett.* **105** 136601
[47] Johnson M and Silsbee R H 2007 Calculation of nonlocal baseline resistance in a quasi-one-dimensional wire *Phys. Rev. B* **76** 153107
[48] Mazin I I 1999 How to define and calculate the degree of spin polarization in ferromagnets *Phys. Rev. Lett.* **83** 1427
[49] Kochan D, Gmitra M and Fabian J 2014 Spin relaxation mechanism in graphene: resonant scattering by magnetic impurities *Phys. Rev. Lett.* **112** 116602
[50] Carr S, Massatt D, Fang S, Cazeaux P, Luskin M and Kaxiras E 2017 Twistronics: manipulating the electronic properties of two-dimensional layered structures through their twist angle *Phys. Rev. B* **95** 075420
[51] Hennighausen Z and Kar S 2021 Twistronics: a turning point in 2D quantum materials *Electron. Struct.* **3** 014004
[52] Zollner K, Faria Junior P E and Fabian J 2019 Proximity exchange effects in $MoSe_2$ and WSe_2 heterostructures with CrI_3: twist angle, layer and gate dependence *Phys. Rev. B* **100** 085128
[53] Zollner K and Fabian J 2021 Bilayer graphene encapsulated within monolayers of WS_2 or $Cr_2Ge_2Te_6$: tunable proximity spin-orbit or exchange coupling *Phys. Rev. B* **104** 075126
[54] Zollner K, João S a M, Nikolić B K and Fabian J 2023 Twist- and gate-tunable proximity spin-orbit coupling, spin relaxation anisotropy and charge-to-spin conversion in heterostructures of graphene and transition metal dichalcogenides *Phys. Rev. B* **108** 235166
[55] Li Y and Koshino M 2019 Twist-angle dependence of the proximity spin-orbit coupling in graphene on transition-metal dichalcogenides *Phys. Rev. B* **99** 075438